

Controllable synthesis and adsorption mechanism of flower-like MoS₂/g-C₃N₄ nanocomposites for removal of methylene blue in water

Zhentao Wang

Northwestern Polytechnical University

Jaafar Hasan

Northwestern Polytechnical University

Jingjing Wang

Northwestern Polytechnical University

Caiwei Zhang

Northwestern Polytechnical University

Waheed Iqbal

Northwestern Polytechnical University

Ninghui Chang

Northwestern Polytechnical University

Chuangang Qin (✉ qinchg@nwpu.edu.cn)

Northwestern Polytechnical University <https://orcid.org/0000-0003-4849-0187>

Research Article

Keywords: Flower-like MoS₂/g-C₃N₄, Adsorption, Methylene blue (MB), Mechanism, Ecological assessment

Posted Date: October 7th, 2021

DOI: <https://doi.org/10.21203/rs.3.rs-924254/v1>

License: © ⓘ This work is licensed under a Creative Commons Attribution 4.0 International License.

[Read Full License](#)

Version of Record: A version of this preprint was published at Journal of Nanoparticle Research on April 1st, 2022. See the published version at <https://doi.org/10.1007/s11051-022-05465-9>.

Abstract

The fabrication and adsorption mechanism of flower-like MoS₂/g-C₃N₄ nanocomposites as new adsorbent materials were investigated by batch sorption experiments in this paper. The influence of factors such as pH, adsorbent dosage, concentration and temperature on the adsorption properties of flower-like MoS₂/g-C₃N₄ nanocomposites were studied in detailed. The adsorption isotherm data was fitted with the Langmuir model, and the adsorption kinetic characteristics conform to the quasi second-order kinetic equation. Thermodynamic data showed that the adsorption process of methylene blue (MB) was feasible, endothermic and spontaneous. At 45 °C, the maximum adsorption capacity was 278.4 mg/g. The adsorbed MB solution was used to water the wheat and chickpea plants within 15 days. Compared with MB solution, the treated MB solution made the plants grow much more better.

1. Introduction

With remarkable industrial development and the continuous growth of the global population, people's demand for textile and clothing is increasing, which resulted in the continuous discharge of distinctive toxic pollutants into the water streams that raises serious environmental problems (Pan et al., 2016). Considering that in the textile, leather and paper industries, about 80% of the dye wastewater is discharged into the water without any treatment every year, which has brought very serious damage to the water supply environment, and has become a major problem that seriously threatens the quality of the biosphere and drinking water supply around the world (Carolin et al., 2017; Katheresan et al., 2018; Oladipo & Gazi, 2014).

Dye wastewater mainly comes from the production industry of dyes and dye intermediates, which is composed of mother liquor of various products and intermediates crystallization, materials lost in the production process and sewage washing the ground, among which organic dye wastewater accounts for a large proportion. Most organic dyes have certain biological toxicity, which can threaten the health of organisms in the water and even cause their death. At present, the commonly used methods for the treatment of printing and dyeing wastewater include photocatalytic degradation (Pang et al., 2018), adsorption (Yu et al., 2018), biological treatment (Wang et al., 2013), filtration (Zanacic et al., 2016) and membrane technology (Farhat et al., 2016). Because the adsorption method is low cost, effective, easy to operate and not easy to cause secondary pollution, it has gradually become an indispensable solution for printing and dyeing wastewater treatment (Gao et al., 2016; Wang et al., 2019). The effect of dye wastewater treatment by adsorption method mainly depends on the adsorbent structure and surface morphology, so the preparation of adsorbent with good adsorption performance is the key to achieve efficient treatment of dye wastewater.

There has been extensive research on the preparation and modification of adsorption materials, among which carbon materials is the most representative. It has a large specific surface area and good adsorption performance, and is the most widely used adsorbent (L. Chen et al., 2017; Manilo et al., 2016; Murray & Ormeci, 2018). More and more attention has been paid to obtaining cheap and easily available

materials with large specific surface area, unique structural properties and excellent chemical stability. Graphite phase carbon nitride is a new type of non-metallic graphite semiconductor material, which has the advantages of good stability, metal-free “earth abundant nature” and many adsorption sites (Wu et al., 2018). It showed excellent application prospects in the field of adsorption (Hu et al., 2015; Zhang et al., 2016). However, the bulk $g\text{-C}_3\text{N}_4$ synthesized directly from organic precursors often has a smaller specific surface area (less than $20 \text{ m}^2 \cdot \text{g}^{-1}$), and meagre mass/diffusion transfer rate. From a practical perspective, particularly in adsorption, the establishment of controlled porosity and morphology at the nanoscale in bulk $g\text{-C}_3\text{N}_4$ is essential to maximize its efficiency. In 2013, Galen D. Stucky and co-workers synthesized carbon nitride mesoporous hollow spheres by changing the precursor materials, which greatly improved the specific surface area and adsorption sites (Jun et al., 2013). MoS_2 , indicating that a large number of sulfides (S^{2-}) can absorb various heavy metal and organic pollutants through electrostatic, hydrophobic or chemical complex interactions (Li et al., 2018; Liu et al., 2019). Ibrahim M. Alarifi and his colleagues synthesized and used MoS_2 adsorption to adsorb Congo red, at 50°C , the maximum adsorption capacity was 80.64 mg/g (Alarifi et al., 2021). Therefore, we assembled MoS_2 onto $g\text{-C}_3\text{N}_4$ to prepare $\text{MoS}_2/g\text{-C}_3\text{N}_4$ nanocomposites which can combine their excellent properties.

As a common organic dye, methylene blue (MB) is widely used in production, life and scientific research. Studying the adsorption of adsorbent on MB waste liquid can provide an economic and effective method for water pollution treatment. In order to obtain a new adsorbent with good adsorption effect on methylene blue, we synthesized flower-like $\text{MoS}_2/g\text{-C}_3\text{N}_4$ nanocomposites via hydrothermal reaction (Scheme 1). According to the experimental results, the flower-like $\text{MoS}_2/g\text{-C}_3\text{N}_4$ nanocomposites have obvious adsorption for MB. Especially at 45°C , the maximum adsorption capacity of the flower-like $\text{MoS}_2/g\text{-C}_3\text{N}_4$ nanocomposites is 278.4 mg/g . This adsorption capacity is better than many adsorbents reported previously. In addition, the adsorption of MB on the nanocomposites has good recyclability, and it still has good stability after five cycles. We studied the factors affecting MB adsorption (pH, adsorbent dose and original MB concentration), the adsorption isotherm model, adsorption kinetics and thermodynamics. Additionally, we introduced the applicability of the report study of the treated solution. The effluent from the MB removal process is then used to water wheat and chickpeas to examine their effects on plant growth.

2. Experimental Section

2.1 Materials

Melamine, cyanuric acid and $\text{Na}_2\text{MoO}_4 \cdot 2\text{H}_2\text{O}$ were from Aladdin Chemical Reagent Co., Ltd (Shanghai, China), dimethyl sulfoxide and thiourea were from Guangdong Guanghua Sci-Tech Co., Ltd (Guangdong, China). All chemical substances were analytically pure.

2.2 Preparation of $g\text{-C}_3\text{N}_4$ hollow sphere

The nanocomposite was synthesized on the basis of Refs (Jun et al., 2013; S. Zhao et al., 2020). First, added 1 g melamine to 50 ml dimethyl sulfoxide (DMSO), added 1 g cyanuric acid to 25 ml DMSO, stirred for 30 minutes to form a solution, and labeled as A and B. Then, in the process of stirring, dropped solution B into solution A and continued stirring for 30 minutes to form white precipitate. After the reaction, the supernatant was discarded, the precipitate washed and centrifuged, dried at 50 °C for 6 h, and ground into powder, named as MCA. Finally, the MCA was heated to 550 °C for 3 h in muffle furnace to obtain spherical g-C₃N₄.

2.3 Preparation of MoS₂/g-C₃N₄ nanocomposites

First, 0.29 g of Na₂MoO₄ · 2H₂O was added in 40 ml water, and form a solution. Subsequently, 0.005 g of polyvinyl pyrrolidone (PVP) was added in the solution and magnetically stirred for 10 min. After that, hydrochloric acid was added to adjust the solution pH to 1. Then, 1.44 g of thiourea was added, and ultrasonic dispersion was carried out for 10 min to form a solution. 0.192 g g-C₃N₄ was put into the solution, and ultrasonic oscillation was carried out for 2 h. Finally, the reaction mixture was transferred to a high-temperature reactor, and reacted at 220 °C for 18 h. After the reaction, the product was washed, centrifuged and dried at 50 °C for 6 h to obtain MoS₂/g-C₃N₄. Pure MoS₂ can be obtained without adding g-C₃N₄.

2.4 The study of plant growth.

First, 10 seeds of wheat and chickpea of the same shape and size were selected and sprouted in wet cotton day and night. And then planted the seeds in the same amount on the test tube with the same amount of MB solution (40 mg/L) and the treated solution (MB solution adsorbed by MoS₂/g-C₃N₄ nanocomposites). After that, these plants' root and bud growth was analyzed in the next 15 days (Gunture, Aggarwal, et al., 2020; Gunture, Kaushik, et al., 2020; Gunture et al., 2019).

2.5 Characterization of materials

The prepared adsorbents were characterized by XRD (Bruker D2 PHASER X) using Cu K α as the irradiation source ($\lambda = 1.5418 \text{ \AA}$). The chemical composition and electronic state of the adsorbents were studied by XPS (Kratos Axis Ultra DLD). The adsorbents' appearance was recorded by FESEM (FEI Verios G4). And the structural details of the adsorbents were confirmed by HRTEM (FEI Talos F200X TEM). BET (3H-2000PS2) of Beishide Instrument Technology Co., Ltd. (Beijing, China) was used to carry out a nitrogen adsorption-desorption experiment on the adsorbent. The UV-Vis spectrophotometer made by Shanghai Jinghua Instrument was used to analyze the absorbance of the solution.

2.6 Adsorption procedure

Different mass of MoS₂/g-C₃N₄ nanocomposites were added into 50 ml MB solution. The different original concentrations were C₀ (mg/L). After that, the solution in the round bottom flask was heated at different temperatures (15°C, 25°C, 35°C, 45°C) with stirring at 300 rpm for about 60 minutes (until adsorption equilibrium was reached). Adjust the solution pH to 1–11 by HCl or NaOH. After adsorption,

centrifugation, take the supernatant. Then, the absorbance of MB at the maximum absorption wavelength (664nm) was measured by UV spectrophotometer, and after the adsorption equilibrium, the equilibrium concentrations were C_e (mg/L), the removal efficiency ($\eta\%$) and equilibrium adsorption capacity (q_e) of MB solution were counted by these formula:

$$\eta(\%) = \frac{C_0 - C_e}{C_0} \times 100\%$$

1

$$q_e = \frac{(C_0 - C_e) \cdot V}{m}$$

2

where V (L) was the volume of MB solution, m (g) was the weight of $\text{MoS}_2/\text{g-C}_3\text{N}_4$ nanocomposites and q_e (mg/g) was the adsorption capacity at equilibrium.

3. Results And Discussion

3.1 Structure characterization

The powder XRD patterns of the $\text{g-C}_3\text{N}_4$, MoS_2 and $\text{MoS}_2/\text{g-C}_3\text{N}_4$ nanocomposites were shown in Fig. 1. In the typical XRD pattern, all diffraction peaks of $\text{g-C}_3\text{N}_4$ correspond to the standard card (JCPDS 87-1526). At 13.2° , the peak value corresponds to the (100) crystal planes, caused by the periodic arrangement of stacking units between layers of $\text{g-C}_3\text{N}_4$. The peak value at 27.5° corresponds to the (002) crystal planes, which is the characteristic peak of the accumulation of graphite like layered structure of $\text{g-C}_3\text{N}_4$ (Lin et al., 2019). The diffraction peaks of pure MoS_2 at 15.1° , 32.7° , 35.2° , 38.8° , 44.2° and 57.3° belongs to the (002), (100), (102), (103), (006) and (110) crystal planes of hexagonal MoS_2 (JCPDS 37-1492), respectively (Ali et al., 2019). From this typical XRD patterns of $\text{MoS}_2/\text{g-C}_3\text{N}_4$ nanocomposites, we can see the peak of MoS_2 clearly, but the peak value of $\text{g-C}_3\text{N}_4$ is very small, which may be due to the nanocomposites contain the relatively low content of $\text{g-C}_3\text{N}_4$. The other possible reason of weak intensity of (002) peak of $\text{g-C}_3\text{N}_4$ may coincides or interfere with the (100) crystal planes of MoS_2 peak. Nevertheless, the diffraction peak intensity of MoS_2 decreases with the addition of $\text{g-C}_3\text{N}_4$, especially at 15.1° peak. This indicates that the addition of $\text{g-C}_3\text{N}_4$ further limits the accumulation of the molybdenum disulfide layer (Y. X. Chen et al., 2017).

XPS analysis further determined the chemical state and element composition of the $\text{MoS}_2/\text{g-C}_3\text{N}_4$ nanocomposites. Figure 2a illustrated the XPS survey spectrum confirmed C, N, Mo, and S elements exist in $\text{MoS}_2/\text{g-C}_3\text{N}_4$ nanocomposites. Figure 2b represents the spectra of C1s, where 284.1 eV corresponds to

the C-C in aromatic rings, 285.8 eV corresponds to N-C = N and 288.0 eV corresponds to C-NH₂ (Yi et al., 2017). Figure 2c suggests that the peaks of N 1s spectra at 398.6 eV, 399.1 eV and 403.8 eV belong to C = N-C, N-(C)₃ and N-H structures, respectively (Cao et al., 2017). In addition, the two peaks in the Mo 3d spectrum at around 228.95 eV and 232.13 eV belong to Mo 3d_{5/2} and Mo 3d_{3/2} in Fig. 2d, respectively. There was another peak of 226.01 eV in this area which is part of S 2s. The spectrum of S 2p in Fig. 2e shows two peaks: 161.87 eV and 163.20 eV were due to s 2p_{3/2} and s 2p_{1/2}, respectively. These studies confirmed the successful preparation of MoS₂/g-C₃N₄ nanocomposites.

The morphology and structures of pure g-C₃N₄, pure MoS₂ and MoS₂/g-C₃N₄ nanocomposites were directly analyzed by SEM and TEM. Figure 3 (a-b) FESEM analysis confirmed that the as prepared g-C₃N₄ possessed the hollow sphere morphology, and Fig. 3a shows that the precursor MCA of g-C₃N₄ is spherical-like. Figure 3b shows the g-C₃N₄ formed after calcination of MCA, which is hollow and spherical. Figure 3c shows pure MoS₂, which is flower-like. Figure 3d indicates that the morphology of the MoS₂/g-C₃N₄ nanocomposites basically keeps the appearance of MoS₂. Figure 3e shows the HRTEM micrograph of MoS₂/g-C₃N₄ nanocomposites. The figure shows that MoS₂ is flower like structure, and g-C₃N₄ is coated by MoS₂. Figure 3f shows the presence of well-defined lattice fringes of 0.62 nm, this can be attributed to the (002) crystal plane of MoS₂ (Monga et al., 2020).

Figure S1 showed the N₂ adsorption desorption isotherm. Since there was almost no adsorption limitation at the high-pressure stage, the adsorption isotherm of MoS₂/g-C₃N₄ nanocomposites was determined to be type-IV isotherm with H3 type hysteresis loops, were closely related to the capillary condensation phenomenon of slit pores generated by the stacking of lamellar particles (Liu et al., 2020; Zhu et al., 2020). The pore size of MoS₂/g-C₃N₄ nanocomposites was mainly between 2–17 nm, this indicates the composite was mesoporous. It can be seen in **Table S1**, the BET surface area, average pore size and pore volume of MoS₂/g-C₃N₄ nanocomposites were 70.656 m²/g, 15.4494 nm and 0.2729 cm³/g, respectively. These sufficient parameters indicated that mesoporous MoS₂/g-C₃N₄ nanocomposites have excellent adsorption properties for MB.

3.2 Experiment majorization

3.2.1 Effect of pH value

The pH value has great influence on the ionization degree of MB molecule and the surface charge of adsorbent in the solution (I et al., 2020). For the sake of studying the effect of pH value on MB adsorption, we set the pH value from 1 to 11. In **Fig. S2**, the MB adsorption efficiency of MoS₂/g-C₃N₄ nanocomposites increased with the pH value in the range of 1 to 11. And the surface charge of MoS₂/g-C₃N₄ nanocomposites was shown in **Fig. S3**. At relatively low pH, the proton ions in the solution may compete with the active sites of cationic dye MB and MoS₂/g-C₃N₄ nanocomposites, which inhibits the adsorption of MB on synthetic adsorbent. With the increase of pH, the surface charge of MoS₂/g-C₃N₄

nanocomposites became lower, resulting in stronger electrostatic attraction between MB and adsorbents. The results showed that the higher the pH value was, the higher the adsorption efficiency was. **Fig. S4** showed that the MoS₂/g-C₃N₄ nanocomposites have higher adsorption efficiency when pH = 7, compared with g-C₃N₄ and MoS₂.

3.2.2 Effect of adsorbent dosage

By adding different amounts of MoS₂/g-C₃N₄ nanocomposites into MB solution, the effects of adsorption dose on adsorption efficiency and adsorption capacity were tested. **Fig. S5** illustrated when the adsorbent Dosage increases, the adsorption efficiency of MB first increases, and then almost remains unchanged, the equilibrium adsorption capacity of MB decreased from 251.2mg/g to 99.7mg/g. This was due to the equilibrium state of the adsorption process, the adsorbent can no longer adsorb MB. It is obvious that a high MB adsorption rate can be achieved even with a small amount of adsorbent. Considering the removal efficiency and practicability, we selected 10mg adsorbent for the following experiments.

3.2.3 Effect of MB concentration

The adsorption capacity and adsorption efficiency of the nanocomposites were tested by adding different concentrations of MB solution. **Fig. S6** showed that when MB concentration increased from 20mg/L to 100mg/L, the equilibrium adsorption capacity increased from 98.8mg/g to 227.4mg/g. It may be that with the increase of MB concentration, the adsorbate in solution has stronger driving force to overcome the mass transfer resistance between solution and adsorbent (L. Zhao et al., 2020). But with the increase of MB concentration, the adsorption rate of MB reduced from 98.80–45.48%, because at a certain concentration, the active center of the adsorbent reached saturation.

3.2.4 Effect of adsorption temperature

In this work, the temperatures were set at 15 °C, 25 °C, 35 °C and 45 °C, respectively. **Fig. S7** showed that temperature had obvious influence on MB adsorption. With the increase of temperature from 15 °C to 45 °C, the adsorption efficiency rose from 86.84–98.17%. Because when the temperature increased, the molecular Brownian motion will accelerate, and low temperature will usually reduce the diffusion rate of MB in the nanocomposites (Fu et al., 2017). Considering the adsorption efficiency and practicability, the following experiments were carried out at 25 °C.

3.2.5 Recyclability of MoS₂/g-C₃N₄ for the MB adsorption

The recyclability and stability of adsorbents can greatly improve efficiency and reduce cost. In this study, MB was desorbed with 0.1mol/L NaOH. **Fig. S8** showed the MB adsorption efficiency of MoS₂/g-C₃N₄ nanocomposites for five consecutive cycles. The results illustrated that the adsorption efficiency of MB decreased gradually because the adsorbate could not be completely desorbed and occupied some active adsorption sites. The adsorption efficiency of the MoS₂/g-C₃N₄ nanocomposite for MB was still 73.58% after five cycles, which showed that the adsorbent has good reusability.

3.3 Adsorption kinetics

Figure 4a showed the effect of contact time on adsorption capacity. With the increase of contact time, the adsorption capacity increased rapidly from the beginning to slowly until the adsorption equilibrium reached 60 minutes. In this study, pseudo-first-order, pseudo-second-order kinetics and intra-particle diffusion models were used to analyze the adsorption process (Tehrani & Zare-Dorabei, 2016). The calculation formula of the pseudo-first-order kinetics model was as follows:

$$\ln(q_e - q_t) = \ln q_e - tk_1 \quad (3)$$

The calculation formula of pseudo-second-order model was as follows:

$$\frac{t}{q_t} = \frac{1}{k_2 q_e^2} + \frac{t}{q_e} \quad (4)$$

The calculation formula of intra-particle diffusion model was as follows:

$$q_t = k_3 t^{0.5} + C \quad (5)$$

Where q_e (mg/g) is described above, q_t (mg/g) represent the adsorption capacity at any contact time, and t (min) is the adsorption time. k_1 , k_2 and k_3 are the pseudo-first-order, pseudo-second-order and intra-particle diffusion model rate constants respectively. C (mg/g) is the intercept obtained by fitting the model of intra-particle diffusion.

The linear fitting results of the two kinetic models were shown in **Fig. 4**. It illustrated that the pseudo-second-order model (**Fig. 4c**) is better than the pseudo-first-order model (**Fig. 4b**) in describing the process of adsorption kinetics, which is proved by the higher R^2 ($R^2 = 0.9999$) value. In addition, the calculated results of the two kinetic models were shown in the **Table S2**. Theoretical equilibrium adsorption capacity q_e (cal) of the pseudo-second-order model is more consistent with the experimental data q_e (exp), which indicates that the adsorption of MB on $\text{MoS}_2/\text{g-C}_3\text{N}_4$ nanocomposites conforms to the pseudo-second-order model, and the adsorption process is mainly controlled by chemical adsorption (Fang et al., 2018; Guan et al., 2017).

The model of intra-particle diffusion after fitting is shown in (**Fig. 4d**). The graph was nonlinear, which proved that intra-particle diffusion was not the only factor limiting particle diffusion. There are three processes for MB adsorption. The first stage was from the solution to the surface of $\text{MoS}_2/\text{g-C}_3\text{N}_4$ nanocomposites. The second stage was the diffusion of MB in $\text{MoS}_2/\text{g-C}_3\text{N}_4$ nanocomposites. The third stage was the final balance stage. The above analysis showed that the intra-particle diffusion and surface adsorption occur simultaneously, which affects the adsorption of MB significantly.

3.4 Adsorption isotherm

Figure S9 showed the MB adsorption isotherms of MoS₂/g-C₃N₄ nanocomposite at different temperatures. The experimental data were fitted into Langmuir model for monolayer adsorption (Eq. (6)) and Friedrich model of multilayer adsorption (Eq. (7)) (Gunture, Kaushik, et al., 2020). They can be expressed as:

$$\frac{C_e}{q_e} = \frac{C_e}{q_m} + \frac{1}{K_L q_m} \quad (6)$$

$$\log q_e = \log K_F + \left(\frac{1}{n}\right) \log C_e \quad (7)$$

where C_e (mg/L) was the equilibrium concentration of MB, q_m (mg/g) was the theoretical maximum adsorption capacity, K_L (L/mg) and K_F were Langmuir constant and Friedrich constant, respectively. n was the constant related to the surface inhomogeneity of adsorbent (L. Zhao et al., 2020).

The fitting results of the two isotherm models were shown in Fig. 5. The datas in Table 1 showed that R^2 values in the Langmuir model (Fig. 5a) were bigger than those in the Friedrich model (Fig. 5b). Therefore, the adsorption of MB on MoS₂/g-C₃N₄ nanocomposites followed the Langmuir isotherm model. At 45 °C, q_{\max} is 278.4 mg/g, which indicates that MoS₂/g-C₃N₄ nanocomposites has higher MB adsorption effect. The comparison of q_{\max} of different adsorbents is given in **Table S3**. Therefore, the adsorption capacity of MoS₂/g-C₃N₄ nanocomposites for MB was similar or higher than that of other commonly used adsorbents.

We use the separation coefficient R_L to evaluate the feasibility of adsorption by the following equation:

$$R_L = \frac{1}{1+K_L C_0} \quad (8)$$

Where C_0 (mg/L) and K_L (L/mg) had explained above. As shown in **Table S4**, we observed that $0 < R_L < 1$, it indicated that the process of MB adsorption was favorable (Mohammadnejad et al., 2018).

Table 1. Modeling parameters of adsorption isotherm calculated by Langmuir model and Freundlich model.

Temperature (°C)	Langmuir			Freundlich		
	q_m (mg/g)	K_L	R^2	K_F	n	R^2
15	197.6	1.13199	0.9986	123.22	7.87216	0.91762
25	228.8	1.25215	0.9989	142.94	7.62660	0.85205
35	257.7	1.31973	0.9991	156.15	6.96913	0.90784
45	277.0	1.54274	0.9985	170.56	6.92617	0.86750

3.5 Adsorption thermodynamics

At different temperatures, we used various thermodynamic parameters to understand the adsorption process. The thermodynamic parameters can be obtained by the following expression:

$$k_L = \frac{q_e}{C_e} \quad (9)$$

$$\Delta G^\theta = -RT \ln K_L \quad (10)$$

$$\ln K_L = \frac{\Delta S^\theta}{R} - \frac{\Delta H^\theta}{RT} \quad (11)$$

Where K_L is the equilibrium distribution coefficient, R is the molar gas constant ($8.314 \text{ J/mol}^{-1} \cdot \text{K}^{-1}$), T (K) is the temperature, ΔG^θ is the Gibbs free energy change, ΔH^θ is the enthalpy change, ΔS^θ is entropy change. Figure 6 showed the plot of $\ln K_L$ against $1/T$. From Table 2 we can see that the value of ΔG^θ was negative, indicating that the adsorption process was a spontaneous process at different temperatures, and the increase in temperature was conducive to the adsorption of MB. The value of ΔH^θ was positive, indicating that the adsorption was an endothermic process. In addition, the value of ΔS^θ was positive which indicated that the disorder of the solid-liquid interface increases during the adsorption process.

Table 2. Thermodynamic parameters for adsorption of MB by $\text{MoS}_2/\text{g-C}_3\text{N}_4$ nanocomposites.

Temperature (°C)	Thermodynamic parameters		
	ΔG^θ (kJ·mol ⁻¹)	ΔH^θ (kJ·mol ⁻¹)	ΔS^θ (J·mol ⁻¹ ·K ⁻¹)
15	-14.86		
25	-16.22	24.17	135.46
35	-17.57		
45	-18.93		

3.6 Ecological assessment of treated wastewater

In order to evaluate the ecological characteristics of the treated MB solution, the untreated MB solution and the treated solution were used for the culture of wheat and chickpea seeds, respectively [24]. The growth of germinated wheat and chickpea seeds was analyzed in the next 15 days. As shown in Fig. 7a, the average length of wheat seedlings grown with MB solution is 14.7 cm, while that is 17.2 cm under treated solution. As shown in Fig. 7b, the average length of chickpea grown with MB solution is 21.4 cm, and that with treated solution is 43.6 cm. The results showed that MB solution had strong inhibition on root and bud germination of both plants. Compared with untreated MB solution, the treated solution shows a great improvement role for growth of root and bud parts of wheat and chickpea.

3.7 Adsorption mechanism

Figure S10 showed the possible adsorption mechanism of MoS₂/g-C₃N₄. From the above that the adsorption of MB by MoS₂/g-C₃N₄ belonged to Langmuir monolayer adsorption model. The adsorption rate decreased with the increase of adsorption capacity. From the molecular structure of MB and MoS₂/g-C₃N₄, there was an electrostatic interaction between MB and MoS₂/g-C₃N₄ due to that MB is a cationic dye, while MoS₂/g-C₃N₄ is negatively charged in the solution (**Fig. S3**). As shown in Figure S10, MB and MoS₂/g-C₃N₄ both contain aromatic rings and possible stronger π - π interaction. In addition, both MoS₂/g-C₃N₄ and MB contain nitrogen atoms, and hydrogen bonds may be formed between them. The above analysis indicated that the adsorption of MB was mainly driven by electrostatic interactions, together with π - π interaction and hydrogen bond.

4. Conclusions

We designed and synthesized MoS₂/g-C₃N₄ nanocomposites for MB adsorption in this study. The experimental results indicated that it is feasible to remove MB from water by adsorption. The factors affecting the adsorption performance of MB (pH of solution, adsorption dose, MB concentration and adsorption temperature) were studied. The adsorption process followed the Langmuir monolayer adsorption isotherm model and the pseudo second-order kinetic model. Thermodynamic data showed that adsorption is a spontaneous process, and the increase of temperature is conducive to the adsorption

of MB. MB can reach the adsorption equilibrium within 60 min, and the maximum adsorption capacity of MB was 278.4 mg/g at 45 °C. On the other hand, after the treated wastewater was used for watering the seeds of wheat and chickpea, we found that the treated wastewater was more conducive to the growth of wheat and chickpea than MB solution. The present study indicated that the synthesized MoS₂/g-C₃N₄ nanocomposites have good application prospects for waste-water treatment and environmental remediation.

Declarations

Ethics approval and consent to participate: Not applicable

Consent for publication: Not applicable

Declaration of interests: The authors declare that they have no known competing financial interests or personal relationships that could have appeared to influence the work reported in this paper.

Funding: This research received no external funding

Author Contributions: Conceptualization, C.Q.; methodology, Z.W., J.H.; validation, C.Q., Z.W., J.H., N.C.; investigation, Z.W., J.H., J.W., C.Z, C.Q., N.C.; resources, C.Q., N.C.; data curation, Z.W., C.Q., J.H., C.Z., J.W., W.I., N.C.; writing-original draft preparation, Z.W., J.H., C.Q.; writing-review and editing, Z.W., J.H., C.Q., W.I.; supervision, C.Q., N.C.; project administration, C.Q., N.C.; funding acquisition, C.Q., N.C.

Acknowledgments

This work was financially supported by National Natural Science Foundation of China (21572180, 21602174), the Intergovernmental Science and Technology Cooperation and Exchange Program between China and Romania (43-24-20180510), the Natural Science Basic Research Plan in Shaanxi Province of China (2012JZ2002), and Academic Funding of Northwestern Polytechnical University (NPU, 17GH0402, W212002). We gratefully acknowledge the Analytical and Testing Center (ATC) of Northwestern Polytechnical University for providing well-support as SEM, TEM and XRD throughout the research work.

Appendix A. Supplementary data

Supplementary data to this article can be found online at

References

1. Alarifi IM, Al-Ghamdi YO, Darwesh R, Ansari MO, Uddin MK (2021) Properties and application of MoS₂ nanopowder: Characterization, Congo red dye adsorption, and optimization. *J Mater Res Technol* 13:1169–1180. <https://doi.org/10.1016/j.jmrt.2021.05.028>

2. Ali GAM, Thalji MR, Soh WC, Algarni H, Chong KF (2019) One-step electrochemical synthesis of MoS₂/graphene composite for supercapacitor application. *J Solid State Electrochem* 24(1):25–34. <https://doi.org/10.1007/s10008-019-04449-5>
3. Cao YZ, Gao Q, Li Q, Jing XB, Wang SF, Wang W (2017) Synthesis of 3D porous MoS₂/g-C₃N₄ heterojunction as a high efficiency photocatalyst for boosting H₂ evolution activity. *RSC Adv* 7(65):40727–40733. <https://doi.org/10.1039/c7ra06774g>
4. Carolin CF, Kumar PS, Saravanan A, Joshiba GJ, Naushad M (2017) Efficient techniques for the removal of toxic heavy metals from aquatic environment: A review. *J EnvironChem Eng* 5(3):2782–2799. <https://doi.org/10.1016/j.jece.2017.05.029>
5. Chen L, Li YH, Du QJ, Wang ZH, Xia YZ, Yedinak E, Lou J, Ci LJ (2017) High performance agar/graphene oxide composite aerogel for methylene blue removal. *Carbohydr Polym* 155:345–353. <https://doi.org/10.1016/j.carbpol.2016.08.047>
6. Chen YX, Ma WJ, Cai KF, Yang XW, Huang CJ (2017) In Situ Growth of Polypyrrole onto Three-Dimensional Tubular MoS₂ as an Advanced Negative Electrode Material for Supercapacitor. *Electrochim Acta* 246:615–624. <https://doi.org/10.1016/j.electacta.2017.06.102>
7. Fang Y, Huang Q, Liu P, Shi J, Xu G (2018) Easy-separative MoS₂-glue sponges with high-efficient dye adsorption and excellent reusability for convenient water treatment. *Coll Surf A: Physicochem Eng Aspects* 540:112–122. <https://doi.org/10.1016/j.colsurfa.2018.01.001>
8. Farhat NM, Vrouwenvelder JS, Van Loosdrecht MCM, Bucs SS, Staal M (2016) Effect of water temperature on biofouling development in reverse osmosis membrane systems. *Water Res* 103:149–159. <https://doi.org/10.1016/j.watres.2016.07.015>
9. Fu NJ, Li LT, Liu X, Fu NA, Zhang CC, Hu LD, Li DH, Tang BK, Zhu T (2017) Specific recognition of polyphenols by molecularly imprinted polymers based on a ternary deep eutectic solvent. *J Chromatogr A* 1530:23–34. <https://doi.org/10.1016/j.chroma.2017.11.011>
10. Gao Y, Guo Y, Zhang H (2016) Iron modified bentonite: Enhanced adsorption performance for organic pollutant and its regeneration by heterogeneous visible light photo-Fenton process at circumneutral pH. *J Hazard Mater* 302:105–113. <https://doi.org/10.1016/j.jhazmat.2015.09.036>
11. Guan T, Fang L, Lu Y, Wu F, Ling FL, Gao JM, Hu BS, Meng FM, Jin XQ (2017) A facile approach to synthesize 3D flower-like hierarchical NiCo layered double hydroxide microspheres and their enhanced adsorption capability. *Coll Surf A: PhysicochemEng Aspects* 529:907–915. <https://doi.org/10.1016/j.colsurfa.2017.06.049>
12. Gunture, Aggarwal R, Garg AK, Kaushik J, Sonkar SK (2020) Pollutant-based onion-like nanocarbons for improving the growth of gram plants. *Mater Today Chem*, 18, Article 100352. <https://doi.org/10.1016/j.mtchem.2020.100352>
13. Gunture, Kaushik J, Garg AK, Saini D, Khare P, Sonkar SK (2020) Pollutant Diesel Soot Derived Onion-like Nanocarbons for the Adsorption of Organic Dyes and Environmental Assessment of Treated Wastewater. *Indust Eng Chem Res* 59(26), 12065–12074. <https://doi.org/10.1021/acs.iecr.0c01267>

14. Gunture, Singh A, Bhati A, Khare P, Tripathi KM, Sonkar SK (2019) Soluble Graphene Nanosheets for the Sunlight-Induced Photodegradation of the Mixture of Dyes and its Environmental Assessment. *Sci Rep* 9:Article 2522. <https://doi.org/10.1038/s41598-019-38717-1>
15. Hu R, Wang X, Dai S, Shao D, Hayat T, Alsaedi A (2015) Application of graphitic carbon nitride for the removal of Pb(II) and aniline from aqueous solutions. *Chem Eng J* 260:469–477. <https://doi.org/10.1016/j.cej.2014.09.013>
16. I M, Saleh HAM, Qasem KMA, Shahid M, Mehtab M, Ahmad M (2020) Efficient and selective adsorption and separation of methylene blue (MB) from mixture of dyes in aqueous environment employing a Cu(II) based metal organic framework. *Inorg Chim Acta*, 511, Article 119787. <https://doi.org/10.1016/j.ica.2020.119787>
17. Jun YS, Lee EZ, Wang XC, Hong WH, Stucky GD, Thomas A (2013) From Melamine-Cyanuric Acid Supramolecular Aggregates to Carbon Nitride Hollow Spheres. *Adv Funct Mater* 23(29):3661–3667. <https://doi.org/10.1002/adfm.201203732>
18. Katheresan V, Kansedo J, Lau SY (2018) Efficiency of various recent wastewater dye removal methods: A review. *J Environ Chem Eng* 6(4):4676–4697. <https://doi.org/10.1016/j.jece.2018.06.060>
19. Li ZZ, Meng XC, Zhang ZS (2018) Recent development on MoS₂-based photocatalysis: A review. *J Photochem Photobiol C-Photochem Rev* 35:39–55. <https://doi.org/10.1016/j.jphotochemrev.2017.12.002>
20. Lin B, Li J, Xu B, Yan X, Yang B, Wei J, Yang G (2019) Spatial positioning effect of dual cocatalysts accelerating charge transfer in three dimensionally ordered macroporous g-C₃N₄ for photocatalytic hydrogen evolution. *Appl Catal B: Environ* 243:94–105. <https://doi.org/10.1016/j.apcatb.2018.10.029>
21. Liu C, Wang QM, Jia FF, Song SX (2019) Adsorption of heavy metals on molybdenum disulfide in water: A critical review. *J Mol Liquids*, 292, Article 111390. <https://doi.org/10.1016/j.molliq.2019.111390>
22. Liu Z, Chen G, Hu F, Li X (2020) Synthesis of mesoporous magnetic MnFe₂O₄@CS-SiO₂ microsphere and its adsorption performance of Zn²⁺ and MB studies. *J Environ Manage* 263:Article 110377. <https://doi.org/10.1016/j.jenvman.2020.110377>
23. Manilo M, Lebovka N, Barany S (2016) Mechanism of Methylene Blue adsorption on hybrid Iaponite-multi-walled carbon nanotube particles. *J Environ Sci* 42:134–141. <https://doi.org/10.1016/j.jes.2015.06.011>
24. Mohammadnejad M, Hajiashrafi T, Rashnavadi R (2018) An erbium-organic framework as an adsorbent for the fast and selective adsorption of methylene blue from aqueous solutions. *J Porous Mater* 25(3):761–769. <https://doi.org/10.1007/s10934-017-0489-8>
25. Monga D, Ilager D, Shetti NP, Basu S, Aminabhavi TM (2020) 2D/2D heterojunction of MoS₂/g-C₃N₄ nanoflowers for enhanced visible-light-driven photocatalytic and electrochemical degradation of organic pollutants. *J Environ Manage* 274:Article 111208. <https://doi.org/10.1016/j.jenvman.2020.111208>

26. Murray A, Ormeci B (2018) Competitive effects of humic acid and wastewater on adsorption of Methylene Blue dye by activated carbon and non-imprinted polymers. *J Environ Sci* 66:310–317. <https://doi.org/10.1016/j.jes.2017.04.029>
27. Oladipo AA, Gazi M (2014) Enhanced removal of crystal violet by low cost alginate/acid activated bentonite composite beads: Optimization and modelling using non-linear regression technique. *J. Water Proc. Eng.* 2, 43–52. <https://doi.org/10.1016/j.jwpe.2014.04.007>
28. Pan Y, Wang J, Sun C, Liu X, Zhang H (2016) Fabrication of highly hydrophobic organic–inorganic hybrid magnetic polysulfone microcapsules: A lab-scale feasibility study for removal of oil and organic dyes from environmental aqueous samples. *J Hazard Mater* 309:65–76. <https://doi.org/10.1016/j.jhazmat.2016.02.004>
29. Pang H, Huang S, Wu Y, Yang D, Wang X, Yu S, Chen Z, Alsaedi A, Hayat T, Wang X (2018) Efficient elimination of Uvi by polyethyleneimine-decorated fly ash. *InorgChemFront* 5(10):2399–2407. <https://doi.org/10.1039/c8qi00253c>
30. Tehrani MS, Zare-Dorabei R (2016) Competitive removal of hazardous dyes from aqueous solution by MIL-68(Al): Derivative spectrophotometric method and response surface methodology approach. *Spectrochim Acta Part A-Mol Biomol Spectro* 160:8–18. <https://doi.org/10.1016/j.saa.2016.02.002>
31. Wang C-Y, Zeng W-J, Jiang T-T, Chen X, Zhang X-L (2019) Incorporating attapulgite nanorods into graphene oxide nanofiltration membranes for efficient dyes wastewater treatment. *Sep Purif Technol* 214:21–30. <https://doi.org/10.1016/j.seppur.2018.04.079>
32. Wang C, Jiang X, Zhou L, Xia G, Chen Z, Duan M, Jiang X (2013) The preparation of organo-bentonite by a new gemini and its monomer surfactants and the application in MO removal: A comparative study. *Chem Eng J* 219:469–477. <https://doi.org/10.1016/j.cej.2013.01.028>
33. Wu HJ, Li CM, Che HN, Hu H, Hu W, Liu CB, Ai JZ, Dong HJ (2018) Decoration of mesoporous Co_3O_4 nanospheres assembled by monocrystal nanodots on g- C_3N_4 to construct Z-scheme system for improving photocatalytic performance. *Appl Surf Sci* 440:308–319. <https://doi.org/10.1016/j.apsusc.2018.01.134>
34. Yi S-S, Yan J-M, Wulan B-R, Li S-J, Liu K-H, Jiang Q (2017) Noble-metal-free cobalt phosphide modified carbon nitride: An efficient photocatalyst for hydrogen generation. *Appl Catal B: Environ* 200:477–483. <https://doi.org/10.1016/j.apcatb.2016.07.046>
35. Yu S, Yin L, Pang H, Wu Y, Wang X, Zhang P, Hu B, Chen Z, Wang X (2018) Constructing sphere-like cobalt-molybdenum-nickel ternary hydroxide and calcined ternary oxide nanocomposites for efficient removal of U(VI) from aqueous solutions. *Chem Eng J* 352:360–370. <https://doi.org/10.1016/j.cej.2018.07.033>
36. Zanicic E, Stavrinides J, McMartin DW (2016) Field-analysis of potable water quality and ozone efficiency in ozone-assisted biological filtration systems for surface water treatment. *Water Res* 104:397–407. <https://doi.org/10.1016/j.watres.2016.08.043>
37. Zhang Y, Zhou Z, Shen Y, Zhou Q, Wang J, Liu A, Liu S, Zhang YM (2016) Reversible Assembly of Graphitic Carbon Nitride 3D Network for Highly Selective Dyes Absorption and Regeneration. *ACS*

38. Zhao L, Lv W, Hou J, Li Y, Duan J, Ai S (2020) Synthesis of magnetically recyclable g-C₃N₄/Fe₃O₄/ZIF-8 nanocomposites for excellent adsorption of malachite green. *Microchem J* 152:Article 104425. <https://doi.org/10.1016/j.microc.2019.104425>
39. Zhao S, Fang J, Wang Y, Zhang Y, Zhou Y, Zhuo S (2020) Synthesis of carbon nitride hollow microspheres with highly hierarchical porosity templated by poly (ionic liquid) for photocatalytic hydrogen evolution. *Appl Organomet Chem* 34(4), Article e5474. <https://doi.org/10.1002/aoc.5474>
40. Zhu SJ, Xu YP, Zhu ZG, Liu ZQ, Wang W (2020) Activation of peroxymonosulfate by magnetic Co-Fe/SiO₂ layered catalyst derived from iron sludge for ciprofloxacin degradation. *Chem Eng J* 384:Article 123298. <https://doi.org/10.1016/j.cej.2019.123298>

Figures

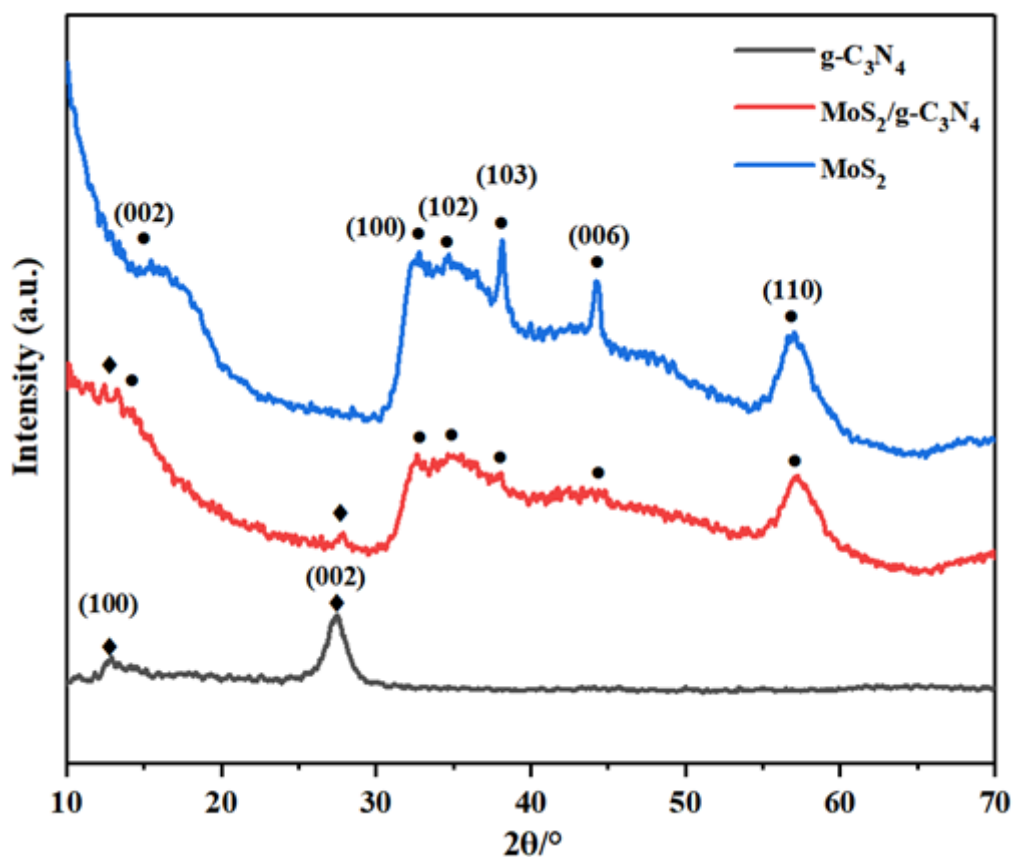


Figure 1

XRD patterns of g-C₃N₄, MoS₂/g-C₃N₄ and MoS₂.

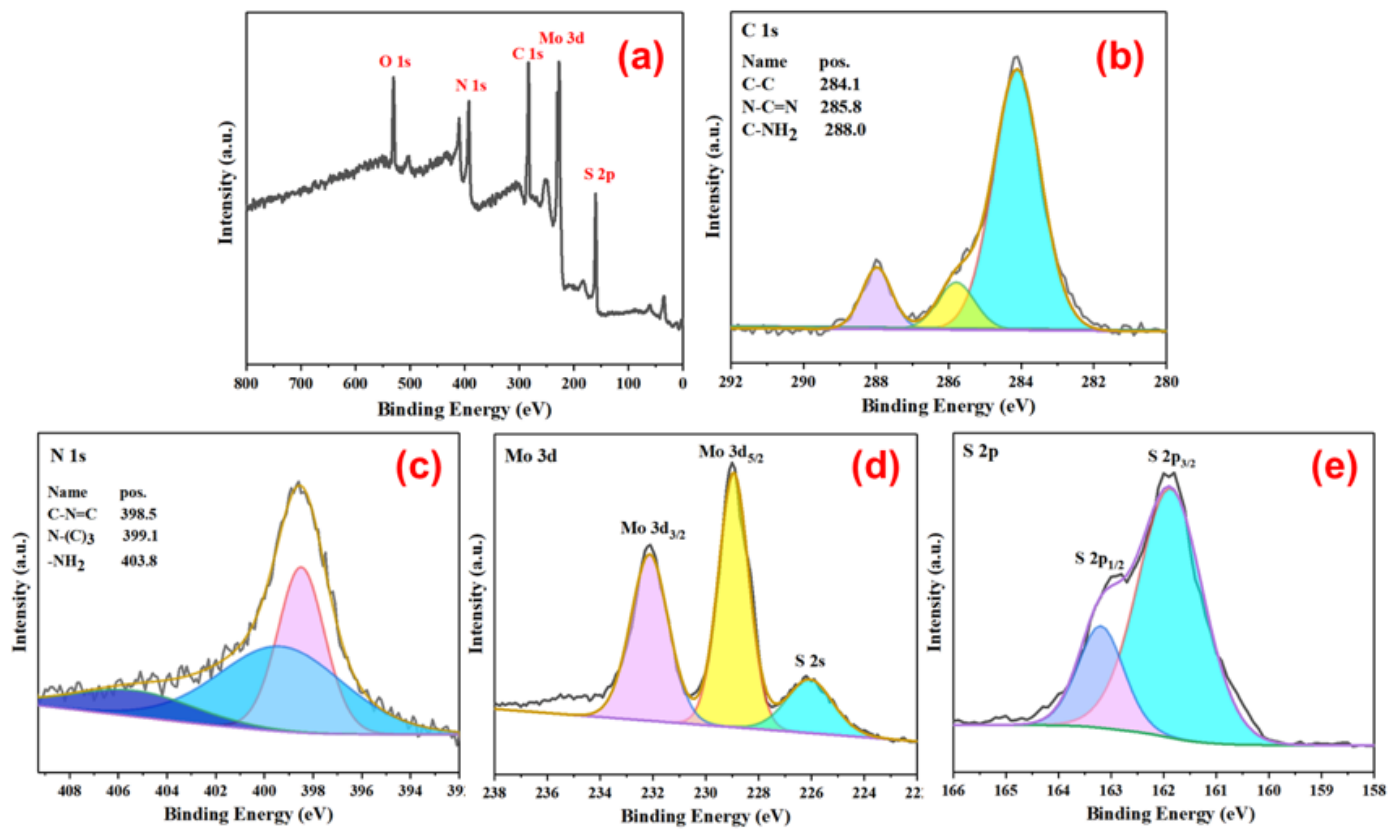


Figure 2

(a) XPS survey scanning of MoS₂/g-C₃N₄. XPS spectra of (b) C 1s, (c) N 1s, (d) Mo 3d and (e) S 2p.

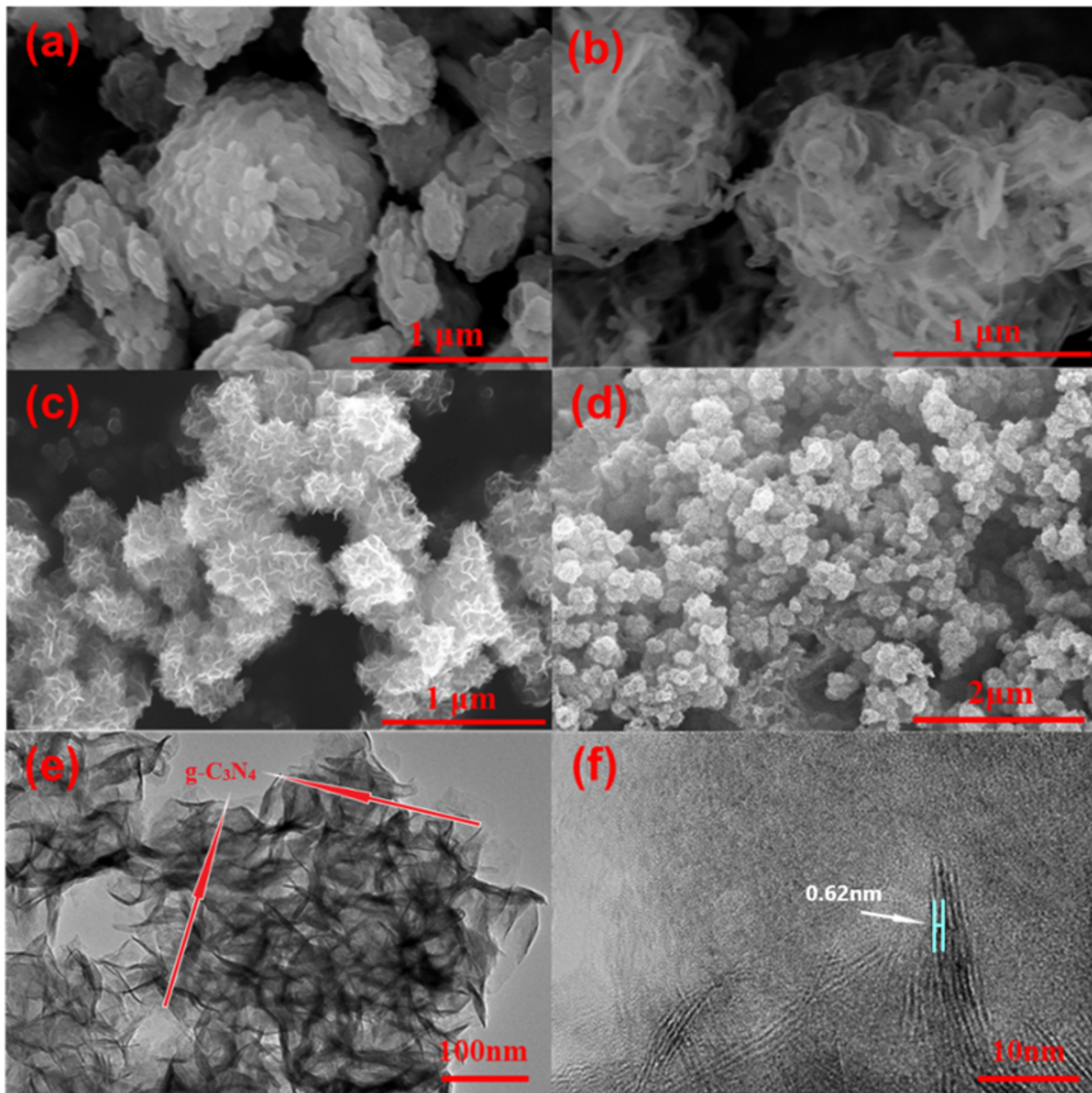


Figure 3

FESEM images of (a) MCA, (b) g-C₃N₄, (c) MoS₂ and (d) MoS₂/g-C₃N₄. HRTEM images of (e-f) MoS₂/g-C₃N₄.

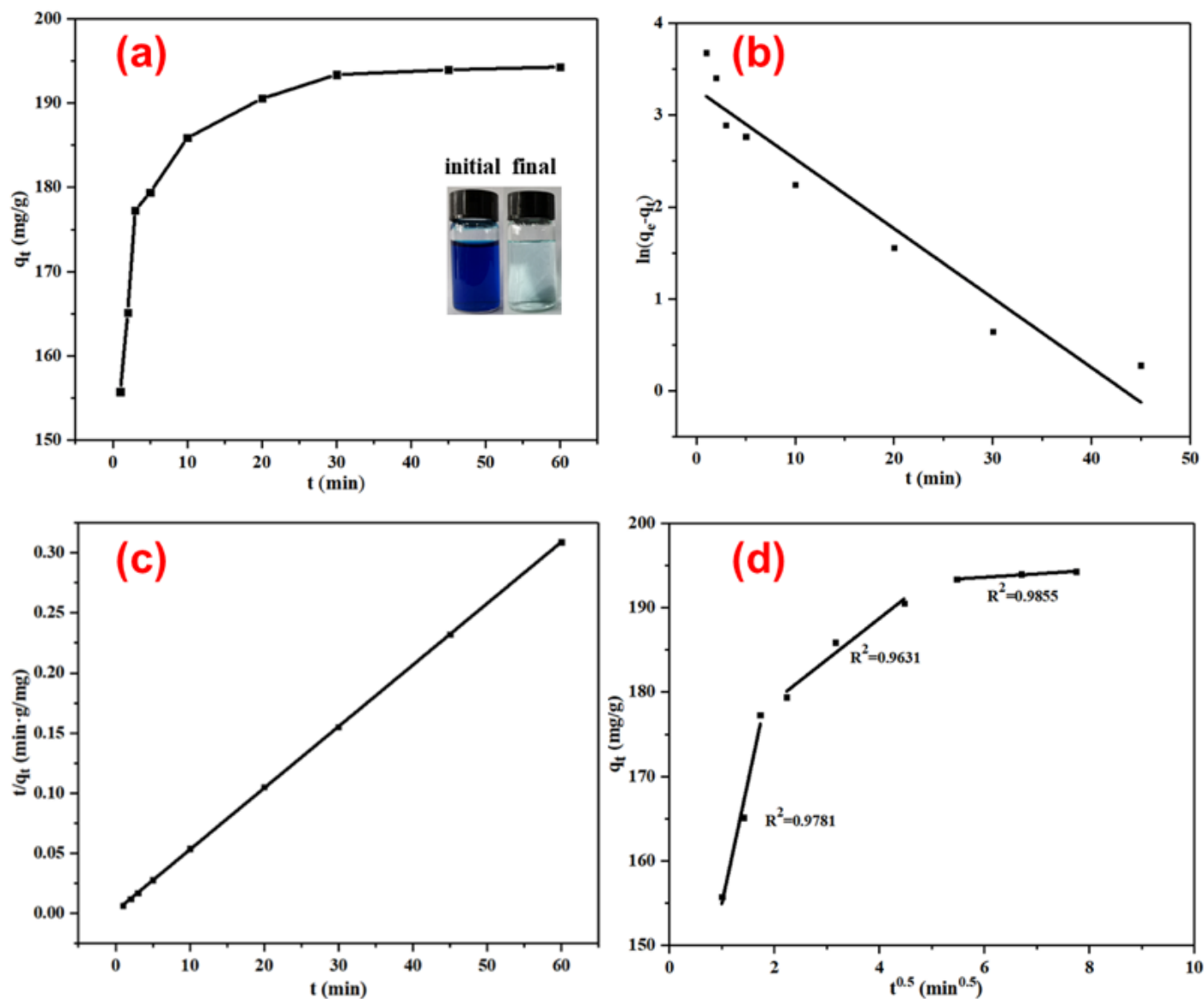


Figure 4

The influence of contact time (a), linear fitted pseudo-first-order model (b), linear fitted pseudo-second-order model (c) and intra-particle diffusion model (d) for MB adsorption by MoS₂/g-C₃N₄ nanocomposites (MB concentration: 100 mg/L, MB volume: 50 ml, adsorbent amount: 25 mg, temperature: 25 °C).

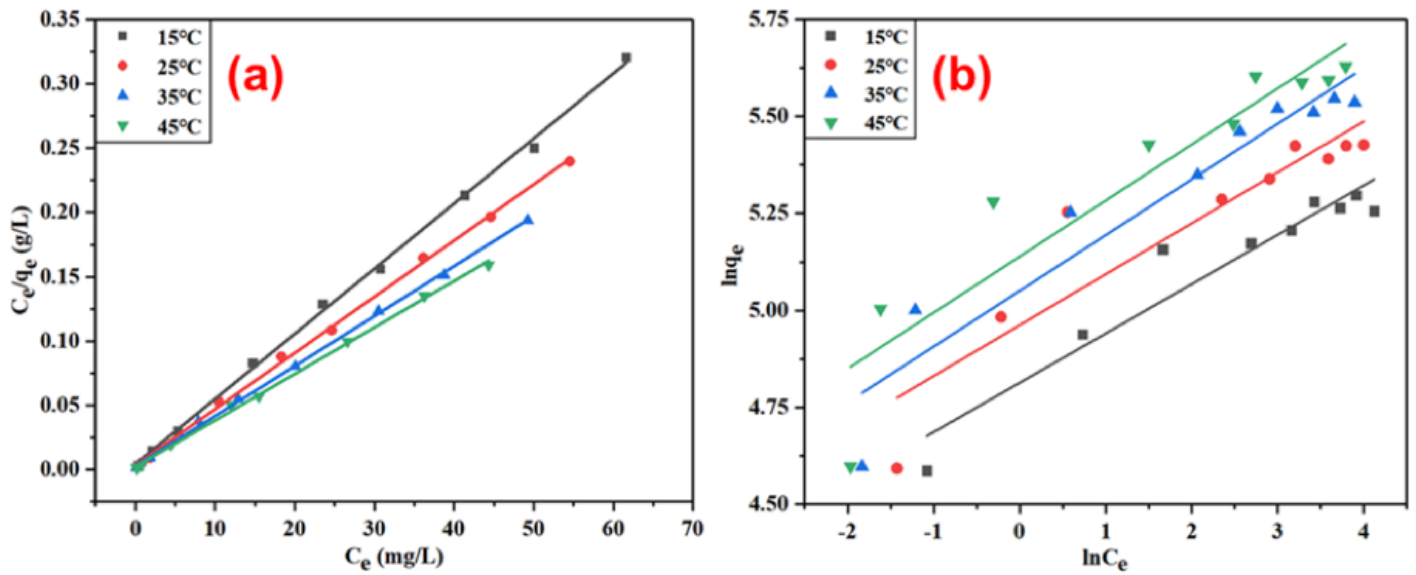


Figure 5

Linear fitted adsorption isotherm models of MB by MoS₂/g-C₃N₄ nanocomposites at different temperatures: (a) Langmuir and (b) Freundlich (MB volume: 50 ml, adsorbent amount: 10 mg).

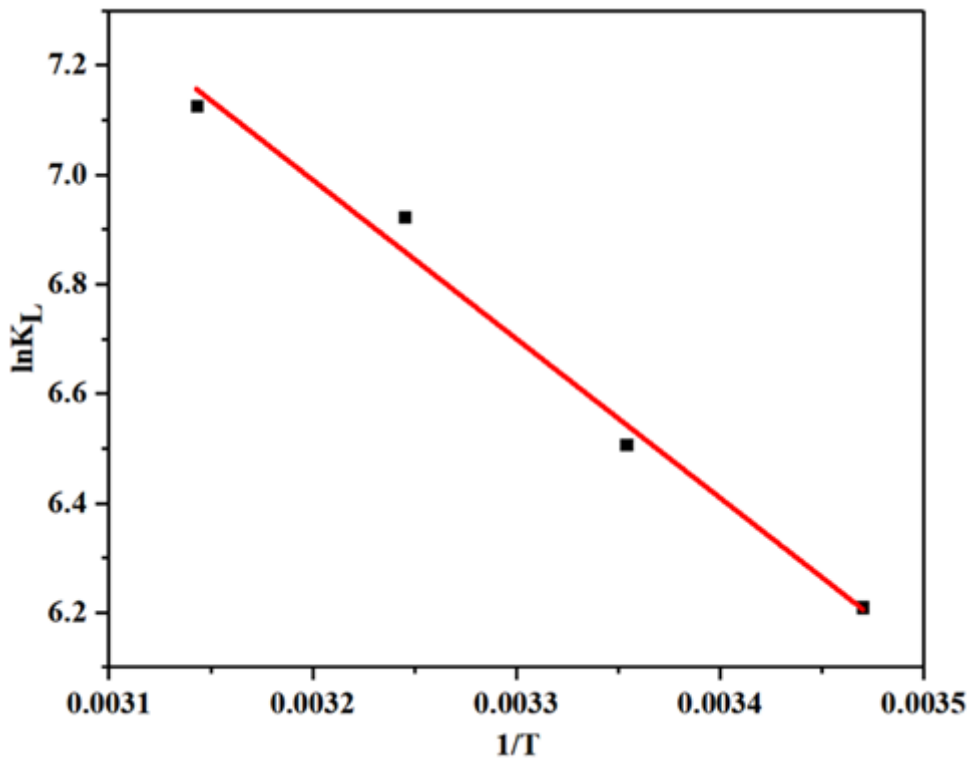


Figure 6

linear fitted thermodynamic plot for MB adsorption (MB volume: 50 ml, adsorbent amount: 10 mg).

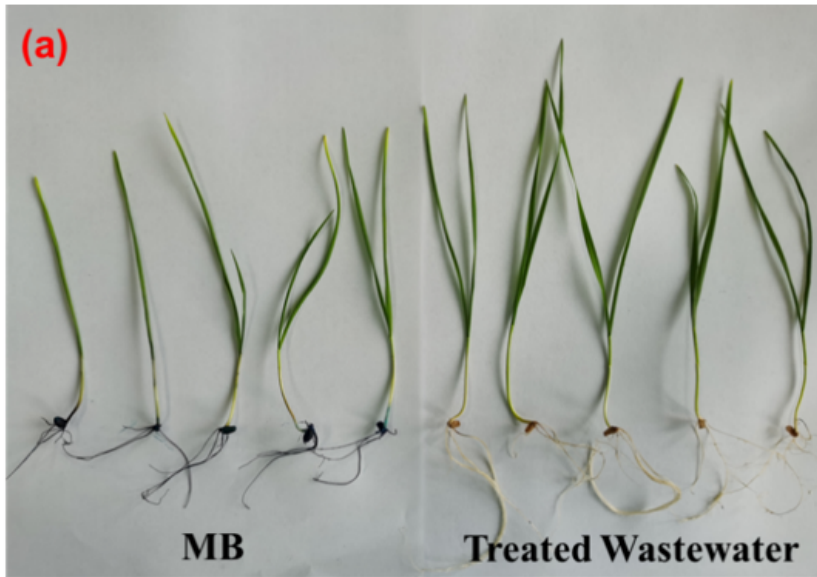


Figure 7

Effect of MB and treated wastewater obtained after adsorption by MoS₂/g-C₃N₄ nanocomposites on (a) wheat plants and (b) Chickpea plants (MB concentration 40 mg L⁻¹; MoS₂/g-C₃N₄ nanocomposites loading 10 mg).

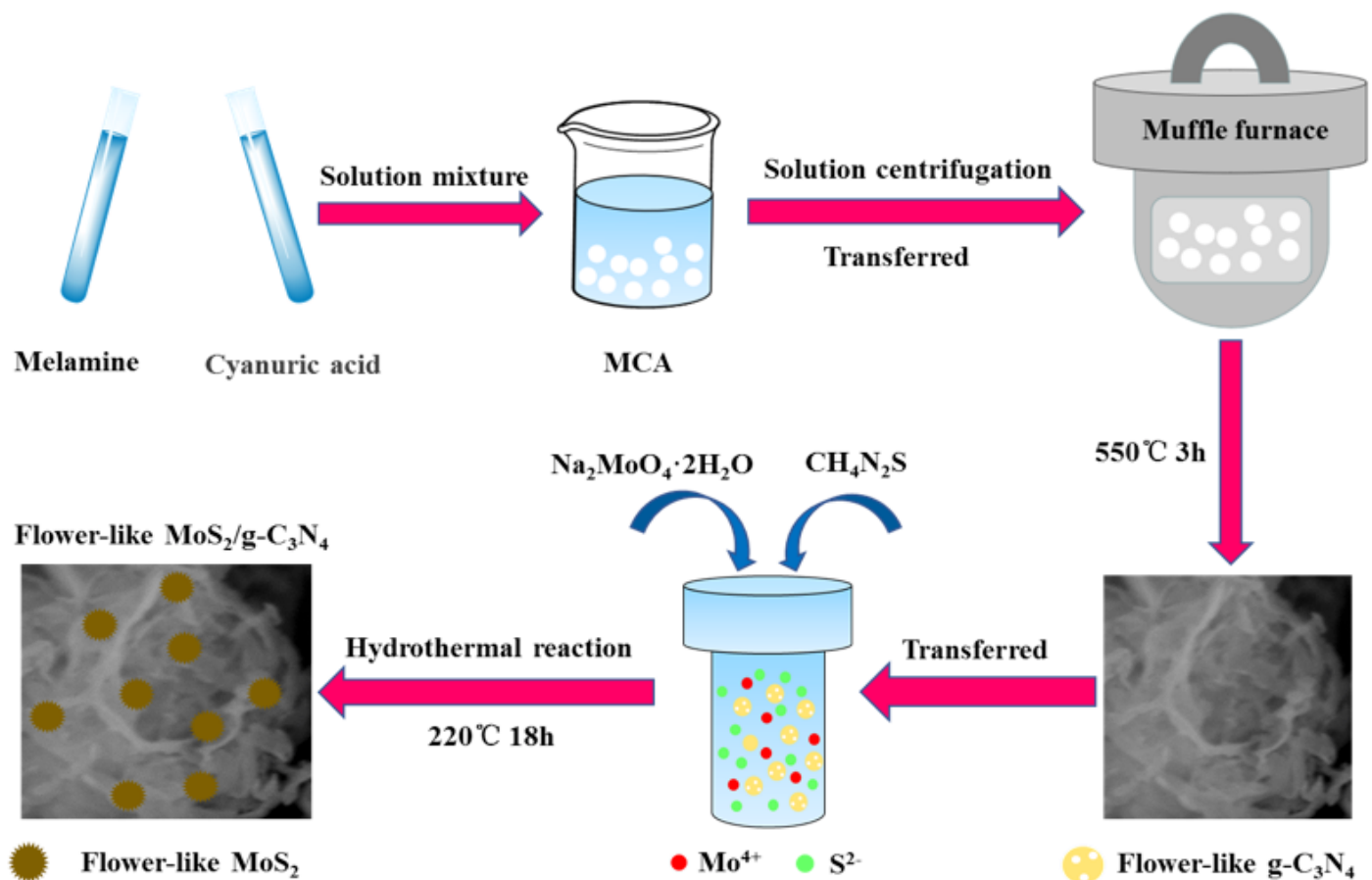


Figure 8

Scheme 1. Schematic diagram for the flower-like $\text{MoS}_2/\text{g-C}_3\text{N}_4$ preparation.

Supplementary Files

This is a list of supplementary files associated with this preprint. Click to download.

- [Graphicabstract.docx](#)
- [SI20210916.pdf](#)